Chapter 5

Chapter 5

Discovery and Characterization of Novel Pyridone and Furan Substituted Ligands of Choline Acetyltransferase

5.1. Introduction

AD is one of the most predominant neurodegenerative diseases (1). Amyotrophic lateral sclerosis (ALS) is another example. A common denominator among these two neurodegenerative diseases is the degeneration of the neuronal cholinergic system, which in case of AD occurs in central cholinergic system, while in ALS the upper and lower motor neurons, and eventually the cholinergic cranial nerves (forming the parasympathetic nervous system) and their interfaces at the neuromuscular sites. These two neurodegenerative diseases alone constitute major challenges and tremendous unmet needs, in term of effective tools for clinical and/or research purposes. This is perhaps one of the reasons why despite the intensive search for the past half century only symptomatic treatments are currently available. Nonetheless, both diseases are complex multifactorial diseases, making it highly challenging to find a cure (2-4).

Cholinergic hypotheses exist for both diseases. In AD, the decline in the key cholinergic neurotransmitter, acetylcholine (5). In ALS, the "dying-back" hypothesis suggest ALS is a distal axonopathy that pathological changes occur prior to motor neuron degeneration and the onset of clinical symptoms (4). Noteworthy, AD and ALS share also other common features. For example, distal cholinergic axonopathy has been also observed in AD (4). Vice versa, amyloid precursor protein (APP) expression and metabolism in muscles seems to also affect function and survival of motoneurons (4). Noteworthy, although ChAT inhibitors are not useful for development of therapeutics for AD or ALS but selective inhibitors of ChAT can be a legit theragnostic candidates for certain cancers, such as colon and lung cancer where acetylcholine is used as an autocrine growth factor through overexpression of ChAT (6, 7).

Overall, discovery of novel and selective ligands for ChAT is of utmost importance for providing us with tools that can increase our understanding and accelerating research on early pathological events affecting the diverse cholinergic neurons, as well as for aiding in early phase diagnosis of the onset of a spectrum of neurodegenerative disorders, in which cholinergic dysfunction is one of the key feature of the disease, such as AD, (8) Lewy body disorder (LBD, including Parkinson's dementia), Down's syndrome (9-12) and ALS (13, 14).

In our initial study (**Chapter 3**), we deduced how the PPIs interact and bind at atomic level with ChAT binding tunnel and inhibit it. Since PPIs are already patented and is a FDA approved drug for gastroesophageal reflux disease and uncomplicated or complicated peptic ulcer disease. In our second study (**Chapter 4**), we explored the piperidine scaffold of the previously identified hit compound B4 with the help on in-silico virtual screening from our lab. We synthesized a series of 60 novel compounds and tested in-vitro and with the successful findings of the second study, we were motivated to design our present study, where we aim to identify novel molecules that have good binding potential against ChAT using high throughput structure-based virtual screening of a large library and further testing *in-vitro* for its inhibitory activity and selectivity towards ChAT. The best performing hit molecule were then analyzed for its binding mode interactions and subjected to 200 ns molecular dynamics simulation in order to understand its dynamic behavior. Thus, such novel hit molecules along with our previously reported compounds hold the potential to be further explored using SAR studies to develop a potent lead compound possessing high affinity, selectivity and optimal physicochemical properties which can be used as molecular probes in PET imaging for mapping the ChAT distribution in the brain for the early phase diagnosis of the health of cholinergic neurons in neurodegenerative diseases like AD.

5.2. Objectives

The objectives of this study are as follows:

- **Structure based virtual screening:** To virtually screen a small molecule library of ~1.4M compounds library using high-throughput docking protocol against ChAT.
- **In vitro biological evaluation:** The obtained virtual hits were then be procured and tested in-vitro using fluorometric ChAT activity assay to validate our findings. To determine the ChAT selectivity, in-vitro activity assays on the anti-targets AChE and BuChE were also performed.
- **In vitro cytotoxicity assay:** To perform the in vitro cytotoxicity assay for the purpose of assessing the cytotoxic properties of specific hit molecules.
- **In silico studies:** To perform molecular docking against ChAT followed by extensive molecular dynamics simulation study to evaluate the binding mode of the compound with the target.

5.3.Result and Discussion

5.3.1. Structure based virtual screening identified several potential ChAT inhibitors

The potential applicability of brain imaging has been ever-expanding rapidly with newer and novel techniques of image acquisition and analysis, enhancing our ability to study and diagnose AD enabling quicker therapeutic interventions. The unpredictability in the clinical diagnosis of AD and ALS has motivated researchers to search novel diagnostic marker compounds. A decisive diagnosis is still necessary and requires a histopathological conformation which is not logical due to the inaccessibility of the brain which makes imaging the key to access the brain. The pursuit for the search of therapeutics that can arrest the course of AD or ALS is the most important challenge to be faced. In AD field, various biomarkers have been developed targeting Aβ like 18F-fluorodeoxyglucose (FDG)(15), 11C-labeled Pittsburg Compound B (11C-PiB) (16) or targeting tau like 18F-flortaucipir for PET imaging (17). Although, the scientific

advancement in neuroimaging limitations still exists related to specificity of the biomarkers (18). Therefore, calls for more definitive and robust biomarker targeting the key pathophysiological pathway in neurodegenerative diseases like AD and ALS. ChAT is positively one such novel target in both AD and ALS pathophysiology, given that degeneration of cholinergic neurons is an early and progressive pathological feature of these two diseases. However, suitable ligands with appropriate properties are lacking. In previous reports, from the FDA database, we identified several PPI, displaying great high potency as ChAT inhibitors (19). The insights on the mechanism of action of these ligands has revealed that the interaction of PPI's pyridine ring with the HIS324 amino acid residue of the catalytic domain of ChAT is crucial for their effect (20). In another work we screened the Asinex database and reported three novel and selective ChAT inhibitors, previously from our research group (21).

Nonetheless, despite superior selectivity and high potency these ligands may lack enough BBB permeability required for accessing ChAT in CNS. Therefore, the primary objective of the present study was to identify novel selective ChAT ligands with favorable BBB permeability. For this, the data of 1.4 million compounds from VitasM chemical library was curated for BBB permeability based on a modified Lipinski's rule of five. The library was also searched for pan assay interference compounds (PAINS) for exclusion of compounds to prevent false positive hits. Finally, the number of potential hits was reduced to 769609 compounds, which were subjected to docking using VinaMPI virtual screening protocol (22). The score cutoff was set to ≥ -10 kcal/mol, leading to selection of 5958 compounds with docking scores as high as -12 kcal/mol. An overview of the virtual screening protocol is shown in (**Figure 5.1**).

High throughput structure-based virtual screening can rapidly identify best performing biologically active hit compounds in an efficient and cost-effective manner. However, a major limitation of these docking analyses is the inevitable gross approximation of the expected property (23, 24). Therefore, it is necessary to validate the screening results and prevent loss of

any crucial hit once the library size have become manageable size. Here, virtual screening results obtained from the VinaMPI yielded 5958 hits that were rescored using XP docking protocol in Glide module available in Maestro for cross platform validation, concerning the robustness of the docking results (25). This approach narrowed down the hits to 250 top scoring compounds with Glide score of -10.953 to -7.379 kcal/mol. These top hits were then subjected to molecular mechanics, i.e., general born surface area (MM/GBSA) binding free energy calculation which uses force-field based scoring functions that requires a higher degree of calculation. This in turn increases the accuracy of hit prediction. MM/GBSA analyses together with manual inspection of the binding pose and interactions resulted in selection of 46 top compounds with scores ranging from -68.42 to 10.92 kcal/mol for *in-vitro* screening evaluation (**Table 5.1**).

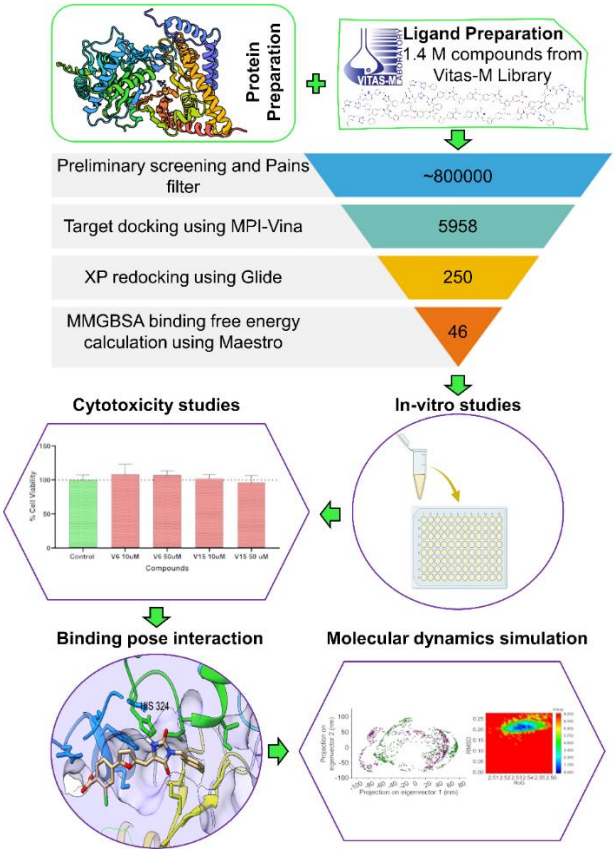

Figure 5.1. Overview of the structure-based virtual screening protocol for the 1.4 million VitasM compound library using VinaMPI for potential hits identification against ChAT.

The compound library was subjected to preliminary screening based on physicochemical parameters and PAINS filter and then subjected to virtual screening using docking protocol. The resultant top 46 hits were subjected to *in vitro* screening from which compound V6 and V15 emerged as the potential selective inhibitors of ChAT. Furthermore, binding pose analysis and MD simulations were carried out to investigate its complex formation with ChAT.

Table 5.1. List of top 46 compounds along with their VitasM codes and SMILES.

Compound ID	**VitasM codes**	**SMILES**
V1	STK214797	Clc1ccc(cc1)C(=O)CC1(O)C(=O)N(c2c1cccc2)Cc1ccc2c(c1)OCO2
V2	STK388849	Clc1ccc(cc1)C(=O)COC(=O)c1ccc2c(c1)C(=O)N(C2=O)c1cccc2c1ccc n2
V3	STK895919	O=C(Nc1cccc(c1)C)COc1cccc(c1)c1noc(n1)COc1ccc(cc1)F
V4	STL083128	O=C(Cn1cccc(c1=O)c1onc(n1)c1ccc(cc1)C)NCCc1ccccc1
V5	STL108088	O=C(Cn1cc(ccc1=O)c1onc(n1)c1cccc(c1)C)NCCC1=CCCCC1
V6	STK161404	Fc1ccc(cc1)CN1C(=O)N/C(=C\c2ccc(o2)c2ccc(c(c2)Cl)C(=O)O)/C1 =O
V7	STK175247	COc1cc(ccc1OCc1cccc(c1)F)/C=C/1\C(=O)NC(=O)N(C1=O)c1ccc(c (c1)Cl)C
V8	STK170827	OC(=O)c1ccc(cc1)COc1ccc(cc1)/C=C/1\C(=O)NC(=O)N(C1=O)c1cc c2c(c1)OCO2
V9	STK219072	Brc1ccc2c(c1)cc(o2)c1nnc(n1C)SCc1nc2ccccc2c(=O)[nH]1
V10	STK223530	O=C(Nc1cccc(c1)Oc1ccc2c(c1)C(=O)N(C2=O)c1ccccc1)CCCC(=O) O
V11	STK156227	Oc1ccc(cc1)C(=O)NN1C(=O)c2c(C1=O)cc(cc2)[N+](=O)[O-]
V12	STK299795	O=C1c2cc(ccc2C(=O)N1NC(=O)c1ccncc1)S(=O)(=O)c1ccc(cc1)C(= O)O
V13	STK094615	COc1cc(ccc1OCCOc1ccccc1)/C=C/1\C(=O)NC(=O)N(C1=O)c1ccccc 1C
V14	STL300279	CN(C(=O)c1ccc(c(c1)Cl)Cl)CCCNC(=O)c1nc2ccccc2c(=O)[nH]1
V15	STK306932	Cc1cc(C)n(c(=O)c1)NC(=O)c1ccn(n1)Cn1nnc(n1)c1ccccc1
V16	STK420897	O=C(c1ccc(o1)C(=O)N/N=C(/c1ccc2c(c1)OCO2)\C)N/N=C(/c1ccc2c (c1)OCO2)\C
V17	STK643610	O=C(N1CCc2c1cccc2)c1ccc2c(c1)s/c(=N/S(=O)(=O)c1ccccc1)/[nH]2

V18	STK640056	O=C(c1onc(n1)c1ccc2c(c1)cc[nH]2)NCC(c1ccccc1)O
V19	STK690288	Brc1ccc(o1)c1noc(n1)C(=O)NCCNC(=O)c1cc2ccccc2oc1=O
V20	STL009303	O=C(NCC(c1ccccc1)O)COc1ccc2c(c1)oc(c(c2=O)Oc1ccccc1)C
V21	STL247594	O=C(Nc1n[nH]c2c1cccc2)CCCCCn1nnc2c(c1=O)cccc2
V22	STL423291	O=C(Nc1ccc2c(c1)OCC(=O)N2C)CCCc1nc(O)c2c(n1)cccc2
V23	STL518544	O=C(COc1cc(O)c2c(c1)OC(CC2=O)(C)C)NCCc1onc(n1)c1ccccc1
V24	STL534544	O=C(C(Oc1cc2oc(=O)cc(c2cc1Cl)C)C)NC(C(=O)O)Cc1c[nH]c2c1cc(O)cc2
V25	STL537500	COc1cccc(c1)/C=C/1\Oc2c(C1=O)ccc(c2)OCC(=O)N[C@@H](C(=O)O)Cc1ccccc1
V26	STL569268	O=C(CC1NC(=O)c2c(N=C1O)cccc2)NCc1onc(n1)c1c(F)cccc1Cl
V27	STL316461	O=C(/N=c/1\[nH]nc(s1)C1CCCO1)CCC1NC(=O)c2c(N=C1O)cccc2
V28	STL536828	O=C(NC(C(=O)O)Cc1c[nH]c2c1cc(O)cc2)COc1ccc2c(c1)oc(=O)c1c2CCC1
V29	STL520058	CC(Oc1ccc(cc1)C(=O)NCCCNC(=O)c1nc(O)c2c(n1)cccc2)C
V30	STL530439	O=C(Cc1c(=O)oc2c(c1C)cc1c(c2)oc2c1CCCC2)N[C@H](C(=O)O)Cc1c[nH]c2c1cccc2
V31	STK806261	O=C(c1ccccc1)N/N=c/1\oc2ccc3c(c2cc1C(=O)N)cccc3
V32	STK642171	O=C(c1ccc2c(c1)s/c(=N/S(=O)(=O)c1ccccc1)/[nH]2)NCc1ccc2c(c1)OCO2
V33	STK607320	CC(C(=O)NCC(c1ccccc1)O)Oc1ccc2c(c1)oc(=O)c1c2cccc1
V34	STK622314	O=C(Nc1cccc(c1)O)COc1ccc2c(c1)occ(c2=O)c1ccc(cc1)Cl
V35	STK631121	O=C(NC1CCCc2c1cccc2)COc1ccc2c(c1)oc(c(c2=O)c1ccccc1)C
V36	STK636132	O=C(COc1ccc2c(c1)c(=O)n1c(n2)CCCCC1)NCCc1ccc(cc1Cl)Cl
V37	STL464257	O=C(COc1ccc2c(c1)oc(=O)c(c2)c1ccccc1)NC[C@@H]1CC[C@H](CC1)C(=O)O
V38	STL160294	COc1ccc(c(c1)F)c1ccc(=O)n(n1)CC(=O)NC(C(=O)O)Cc1ccccc1
V39	STL009364	OC(c1ccccc1)CNC(=O)C1CCN(CC1)C(=O)CNC(=O)c1ccccc1
V40	STK070091	Oc1ccc2c(c1)oc(=O)c(c2)c1csc(n1)c1cc2cc(Cl)ccc2oc1=O
V41	STK494547	Fc1ccc(cc1)C(=O)Nc1cccc(c1)/C(=N/NC(=O)c1cccc(c1)O)/C
V42	STK432350	O=C(c1ccc(cn1)C(=O)NCc1ccc2c(c1)OCO2)NCc1ccc2c(c1)OCO2
V43	STK084803	Clc1ccc(cc1)N1C(=O)NC(=O)/C(=C\c2ccc(cc2)OCCOc2cccc(c2)C)/C1=O
V44	STK079698	COc1cc(ccc1OCc1ccc(cc1)C(=O)O)/C=C\1/S/C(=N\c2ccc(c(c2)C)C)/NC1=O
V45	STK055077	O=C(c1ccc(c(c1)C(=O)O)C(=O)O)c1ccc(cc1)NC(=O)c1ccccc1

V46	STK026652	Oc1ccc(cc1)N1C(=O)c2c(C1=O)cc(cc2)Oc1ccc(cc1)NC(=O)C(F)(F)F

5.3.2. Selection of compound V6 and V15 with *in vitro* ChAT inhibition screening assay

The 46 top scoring hits were purchased and screened *in vitro* for their activity against recombinant human ChAT using a high throughput fluorometric assay, at a single final concentration of 10 µM (**Figure 5.2**). Rabeprazole, one of the PPIs that has been reported by us as a potent ChAT inhibitor was used as a positive control. (19, 20) At the 10µM concentration, rabeprazole inhibited ChAT activity by 100%.

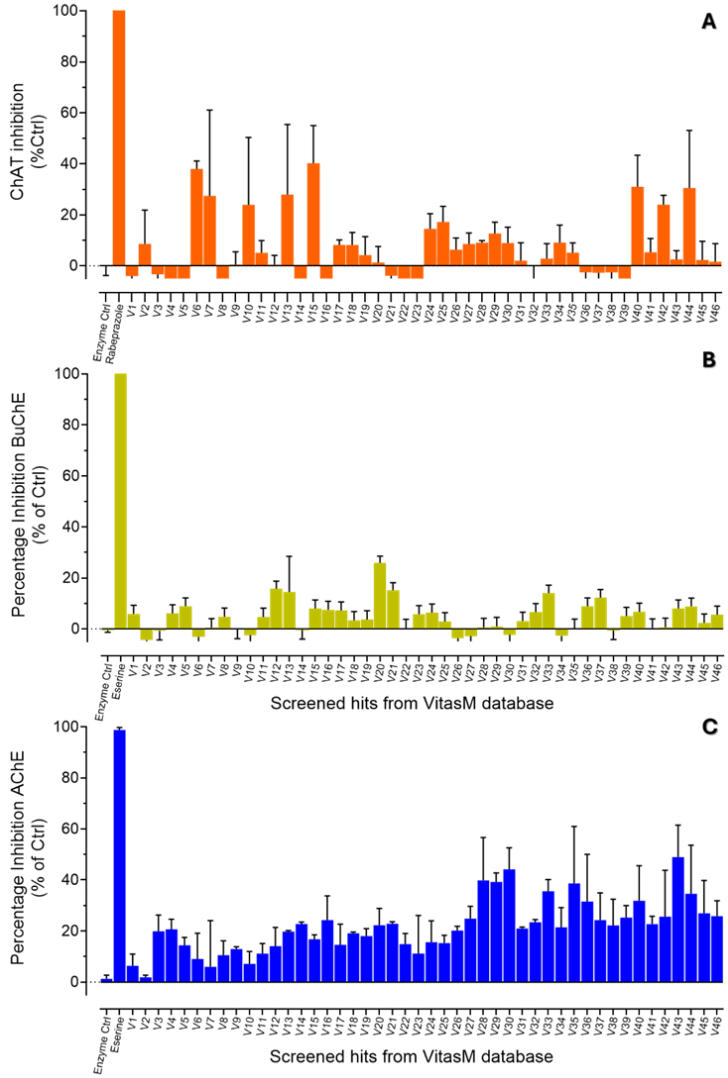

Figure 5.2. Screening of 46 virtual hit compounds for ChAT, AChE and BuChE enzymes inhibition. A) Percentage inhibition of rChAT by virtual hit compounds at 10 µM concentration.

Rabeprazole was used as a positive control and a well without inhibitor containing 0.2% DMSO was used as enzyme control indicating 100 % enzyme activity. **B)** and **C)** Represent the percentage inhibition of rAChE & BuChE by the virtual hit compounds, respectively. Eserine was used as a positive control and a well without inhibitor containing 0.2% DMSO was used as enzyme control indicating 100 % enzyme activity. The data is presented as mean ± SD of an individual experiments performed in six-replicates. The compound with over 40% IR were selected for further kinetic analysis. rChAT = recombinant human choline acetyltransferase; rAChE = recombinant acetylcholinesterase; BuChE = butyrylcholinesterase.

The screening indicated that compound V6 and V15 are good inhibitors of human rChAT with 38.0% ± 3.1% and 40.2% ± 14.9% inhibition of the enzymatic activity respectively (**Figure 5.2A**). We ran simultaneously the compound against two off-targets for ChAT-selective hits, namely BuChE and AChE (**Figure 5.2B and 5.2C, respectively**). Eserine a dual ChE inhibitor, used as the positive control, inhibited both BuChE and AChE by 100%. However, the results showed that compounds V6 and V15 had negligible activity toward BChE and AChE, and thereby were highly selective for ChAT (**Figure 2B and 2C**, and **Table 5.2**). Both compounds were selected for deeper characterization and deduction of their mode of activity by enzyme-inhibition kinetic analyses. There were few other hits with good inhibitory activity against ChAT like compound V7 (27.4% ± 33.7%), V13 (27.9% ± 27.5%), V40 (31% ± 12.4%), V44 (30.5% ± 22.6%), however higher standard deviation indicated inconsistency as well as the compounds lacked selectivity.

Table 5.2. In vitro inhibitory screening data for the 46 top virtual hits from VitasM library.

Compound ID	**ChAT % IR[a]** (Mean ± SD; n=6)	**AChE% IR[a]** (Mean ± SD, n=6)	**BuChE% IR[a]** (Mean ± SD, n=6)
V1	-4 ± 6.3	6.3 ± 4.6	5.8 ± 3.4
V2	8.6 ± 13.3	1.8 ± 0.9	-4.4 ± 3.8
V3	-3.3 ± 8.6	19.9 ± 6.4	-0.7 ± 3.6
V4	-8.2 ± 6.4	20.7 ± 4.0	6.1 ± 3.4

V5	-10.9 ± 10.1	14.4 ± 3.1	8.8 ± 3.3
V6	**38** ± **3.1**	**9.1** ± **10.1**	**-3.1** ± **3.7**
V7	27.4 ± 33.7	6 ±18.1	0.4 ± 3.6
V8	-19.4 ± 12.2	10.5 ± 5.7	4.7 ± 3.4
V9	0.5 ± 5.0	12.9 ± 0.9	-0.2 ± 3.6
V10	24 ± 26.4	7.1 ± 4.8	-2.5 ± 3.7
V11	5.1 ± 4.8	11.1 ± 4.0	4.7 ± 3.4
V12	0.4 ± 3.7	14 ± 7.4	15.7 ± 3.0
V13	27.9 ± 27.5	19.7 ± 0.5	14.4 ± 14.1
V14	-9.7 ± 5.9	22.7 ± 0.8	-0.4 ± 3.6
V15	**40.2** ± **14.9**	**16.7** ± **1.8**	**8** ± **3.3**
V16	-11.1 ± 6.7	24.3 ± 9.5	7.5 ± 3.3
V17	8.1 ± 2.1	14.6 ± 8.1	7.2 ± 3.3
V18	8.2 ± 4.9	19 ± 0.6	3.3 ± 3.5
V19	4.1 ± 7.3	18 ± 3.0	3.7 ± 3.5
V20	1.3 ± 6.3	22.3 ± 6.6	25.9 ± 2.7
V21	-3.9 ± 4.6	22.9 ± 0.8	15.1 ± 3.1
V22	-7.2 ± 5.4	14.8 ± 4.2	0.1 ± 3.6
V23	-10.9 ± 9.5	11.2 ± 14.9	5.7 ± 3.4
V24	14.5 ± 5.9	15.6 ± 8.4	6.3 ± 3.4
V25	17.2 ± 6.1	15.2 ± 3.1	2.9 ± 3.5
V26	6.3 ± 4.7	20.2 ± 1.7	-3.6 ± 3.7
V27	8.6 ± 4.3	24.9 ± 4.8	-2.8 ± 3.7
V28	9.1 ± 0.9	39.8 ± 16.9	0.6 ± 3.6
V29	**12.7** ± **4.4**	**39.2** ± **3.5**	**0.9** ± **3.6**
V30	**8.9** ± **6.2**	**44.1** ± **8.5**	**-2.3** ± **3.7**
V31	2 ± 7.1	21 ± 0.6	3.1 ± 3.5
V32	-0.1 ± 6.7	23.4 ± 1.1	6.5 ± 3.3
V33	2.8 ± 5.9	35.6 ± 4.6	14 ± 3.1
V34	9.1 ± 6.9	21.4 ± 7.8	-2.7 ± 3.7
V35	5.2 ± 3.8	38.6 ± 22.4	0.2 ± 3.6
V36	-2.6 ± 5.2	31.5 ± 18.5	8.8 ± 3.3
V37	-2.7 ± 6.8	24.3 ±10.7	12.3 ± 3.1
V38	-2.7 ± 8.2	22.2 ± 10.3	-0.6 ± 3.6

V39	-6.5 ± 6.4	25.2 ± 4.8	5 ± 3.4
V40	31 ± 12.4	31.8 ± 13.7	6.7 ± 3.4
V41	5.2 ± 5.5	22.7 ± 3.1	0.3 ± 3.6
V42	24 ± 3.6	25.6 ± 18.1	0.6 ± 3.6
V43	**2.5 ± 3.4**	**49 ± 12.5**	**8 ± 3.3**
V44	30.5 ± 22.6	34.6 ± 19.0	8.8 ± 3.3
V45	2.3 ± 7.4	26.9 ± 12.9	2.3 ± 3.5
V46	1.6 ± 7.1	25.8 ± 6.1	5.6 ± 3.4
Eserine	-	98.8 ± 1.0	100.8 ± 0.0
Rabeprazole	108.2 ± 12.4	-	

Data are presented as % inhibition rate (IR) of ChAT enzyme and its off-target enzymes, AChE and BChE. The screening was done at the single concentration of 10 µM. % IR for ChAT represent mean and SD of four independent experiments. % IR for AChE and BChE is the average and SD for two independent experiments, each with six replicates. rhChAT = recombinant human choline acetyltransferase; rhAChE = recombinant human acetylcholinesterase, BuChE = human plasma butyrylcholinesterase.

Moreover, from the *in-vitro* screening of the 46 hits on anti-targets rAChE and BuChE, we discovered some potential compounds with good selectivity and inhibitory activity towards rAChE. For instance, compound V29, V30 and V43 were highly selective (**Table 5.2**). V43 was the strongest AChE inhibitor as it displayed 49.0±12.5% AChE inhibition in comparison to only 8.0% ± 3.3% and 2.5% ± 3.4% inhibition of BuChE and rChAT, respectively. V30 inhibited human AChE by 44.1± 8.5% but had no or little effect on BChE (-2.3%) or ChAT (8.9± 6.2%). V29 showed 39.2± 3.5% inhibition of AChE and no or little effect on BChE (0.9%) or ChAT (12.7± 4.4%). Thereby, these three compounds are expected to be highly selective potent inhibitor of human AChE. However, given that the focus of this study was on ChAT we did not further analyze these compounds.

5.3.2.1.ChAT inhibition kinetics analyses provided the inhibition constant and the mode of inhibition for V6 and V15

As noted, the in vitro screening analyses indicated that the compound V6 and V15 inhibited

ChAT by 38% and 40.2% with negligible activity for the off-targets. We hence performed full ChAT inhibition kinetic assessment on these two top candidates. The inhibition constant (K_i) and the IC_{50} values are shown in **Figure 3** for V6 and in **Figure 4** for V15, which was calculated based on the dose response curves at wide concentration range of the compound and choline as the enzyme substrate (**Figure 5.3 & 5.4**). The 2D structure of the compound V6 is shown in (**Figure 5.3A**). V6 exhibited a K_i value of 11 µM (with a 95% CI of 8.7-16.2µM) which was estimated by nonlinear regression analysis of the whole dataset (**Figure 5.3B**). The IC_{50} value was 21.73 µM at substrate concentrations ranging between 19 to 300 µM (**Figure 5.3D**). Nonlinear regression statistic suggested that V6 is a mixed-competitive inhibitor of ChAT because its data was fitted best in a mixed model inhibition equation. This was confirmed with Lineweaver-Burk plot (double reciprocal) analyses of the substrate-velocity curves of the rChAT enzyme activity at different substrate concentrations (ranging from 1,56 to 25 µM) with or without inhibitors at specified concentrations (**Figure 5.3C**). The Lineweaver-Burk plots were fitted using the linear regression analysis function of GraphPad Prism 9 software. Reciprocal of rate (1/v) is plotted as a function of reciprocal of substrate concentration (1/S) for various concentrations of V6, which produced straight lines on the graph where the X- and Y-axis intercept represents $-1/K_m$ and $1/V_{max}$, while the slope is represented by K_m/V_{max}. The Lineweaver-Burk plot indicated that the K_m value increases, and the V_{max} value decreases with increasing V6 concentrations, suggesting a mixed model type inhibition of ChAT by V6, in line with the nonlinear regression analyses of the data. The K_m and V_{max} values for all concentrations of V6 were also calculated using the substrate-velocity curves (**Figure 5.3B**), which are presented in (**Table 5.3**).

The corresponding ChAT Inhibition Kinetic analyses for **V15** are shown in **Figure 4**. The 2D diagram for the compound V15 is depicted in **Figure 5.4A**. Nonlinear regression analysis indicated that V15 is a potent ChAT inhibitor with a K_i of 4.4 µM (with a 95% CI of 3.3-5.9µM)

and IC_{50} values of 9.4 µM (**Figure 5.4B** and **5.4C**). In addition, the nonlinear regression statistic suggested that the data for **V15** fitted best in the mixed model equation of GraphPad Prism 9 software. This was confirmed by the Lineweaver-Burk plot analyses (**Figure 5.4D**). Similar to V6, the K_m and V_{max} values for all concentrations of V15 are presented in (**Table 5.3)**, which were calculated using the substrate-velocity curves (**Figure 5.4B**).

Altogether, **V6** and **V15** demonstrated high potencies as selective ChAT inhibitor, with a mode of activity indicating that they can bind to ChAT regardless of the enzyme being free or in complex with its substrate. This means that they are going to have full access to the total binding sites (ChAT molecules), which in turn indicates that the compound will have the highest binding potential determined by the concentration of ChAT, an important property for tracer candidates.

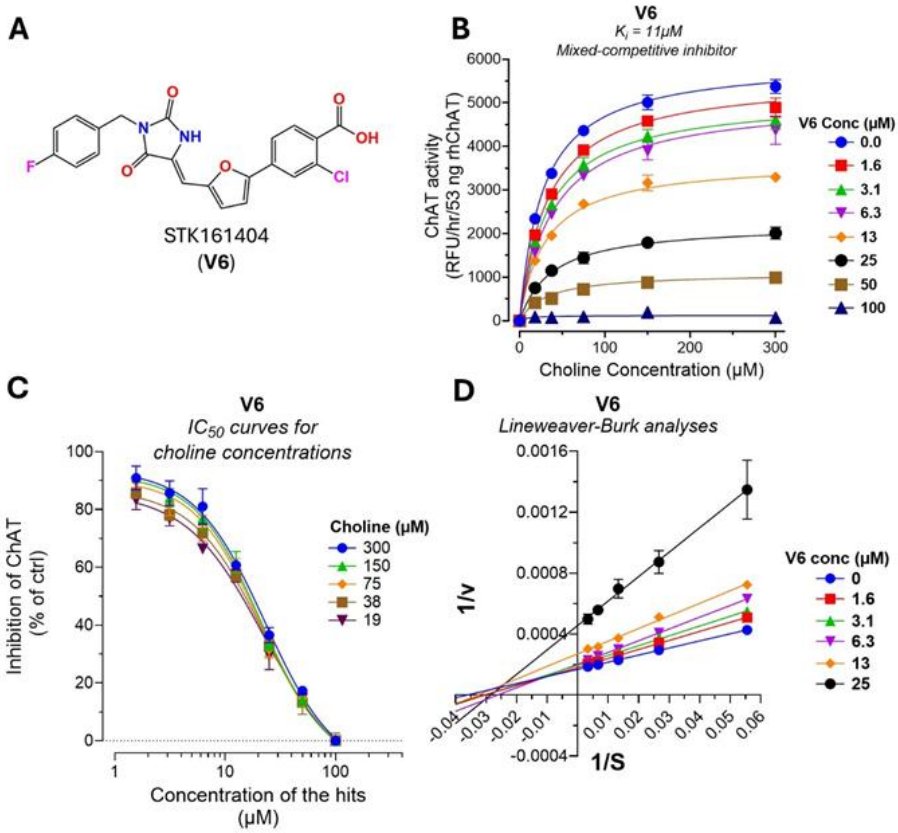

Figure 5.3. ChAT Inhibition Kinetic for compound V6. **A)** Molecular structure of compound V6 (with its catalog no in VitasM Library). **B)** Non-linear regression fitting of the data and the

estimated K_i within the wide range of the substrate concentrations (x-axis) and the V6 concentration range of 1.6 to 100 µM. The analysis was done by fitting and statistically comparing the data based on four different equations in GraphPad Prism 9, namely competitive, non-competitive, uncompetitive and mixed-competitive models. The result indicated that V6 data fitted best as the mixed-competitive inhibition mode of activity compared to all the other models (all $p<0.001$). **C)** Dose-response curves for estimation of IC_{50} of V6 against ChAT at the specified substrate concentrations. The IC_{50} value was calculated after fitting the curves using nonlinear regression function of GraphPad Prism 9. **D)** The Lineweaver-Burk plot analysis for confirmation of the mode of action of V6 as inhibitor of ChAT. The plot was obtained from the substrate-velocity curves of the ChAT enzyme activity at different substrate concentrations and the specified concentration range of V6 (i.e., from 1.6 to 25 µM). The Lineweaver-Burk plots were fitted using the linear regression analysis function of GraphPad Prism 9 software. ChAT = recombinant human choline acetyltransferase.

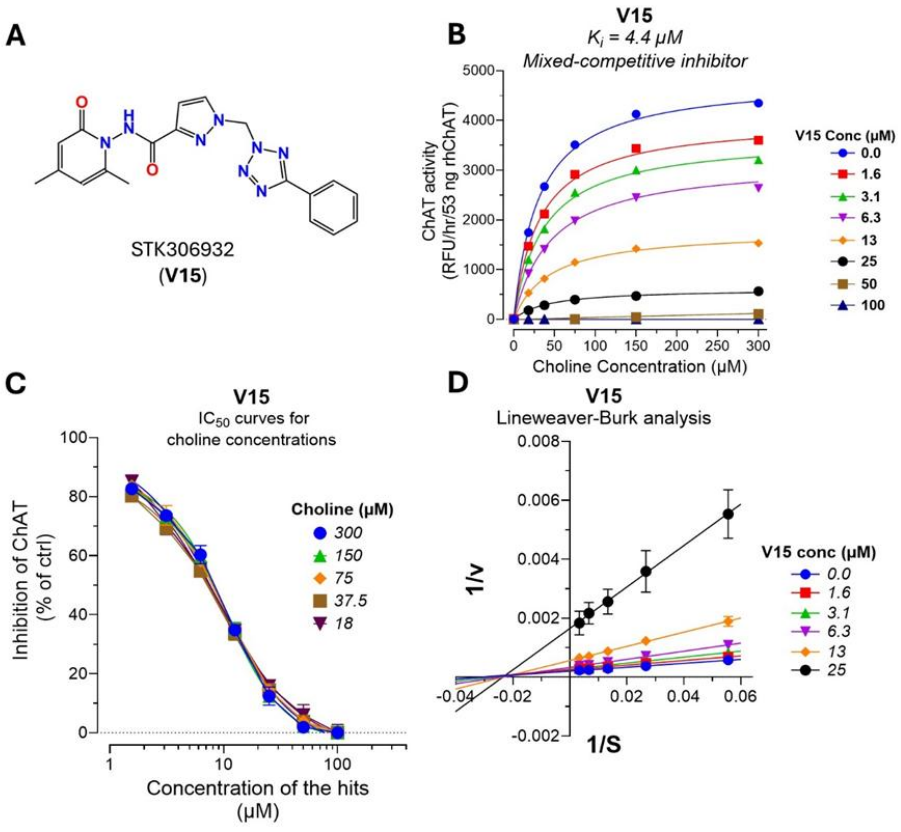

Figure 5.4. ChAT Inhibition Kinetic for compound V15. **A)** Molecular structure of

compound V15 (with its catalog no in VitasM Library). **B)** Non-linear regression fitting of the data and the estimated inhibition constant (K_i) within the wide range of the substrate concentrations (x-axis) and the V15 concentration range of 1.6 to 100μM. The analysis was done by fitting and statistically comparing the data based on four different equations in GraphPad Prism 9, namely competitive, non-competitive, uncompetitive and mixed-competitive models. The result indicated that V15 data fitted best as the mixed-competitive inhibition mode of activity compared to all the other models (all $p<0.001$). **C)** Dose-response curves for estimation of IC_{50} of V15 against ChAT at the specified substrate concentrations. The IC_{50} value was calculated after fitting the curves using nonlinear regression function of GraphPad Prism 9. **D)** The Lineweaver-Burk plot analysis for confirmation of the mode of action of V15 as inhibitor of ChAT. The plot was obtained from the substrate-velocity curves of the ChAT enzyme activity at different substrate concentrations and the specified concentration range of V15 (i.e., from 1.6 to 25 μM). The Lineweaver-Burk plots were fitted using the linear regression analysis function of GraphPad Prism 9 software. ChAT = recombinant choline acetyltransferase.

Table 5.3. The K_m and V_{max} values for compound V6 and V15 at different concentrations, obtained from the ChAT inhibition kinetic analysis performed using GraphPad Prism 7.

Compound	Concentration (μM)	V_{max} (μM /min)	K_m (μM)	R square
V6	0	5908.0 ± 1.37	27.6 ± 62.2	0.988
	1.56	5504.4 ± 1.10	32.74 ± 31.1	0.991
	3.13	5102.2 ± 1.03	32.88 ± 24.7	0.991
	6.25	4932.3 ± 1.04	38.07 ± 17.2	0.993
	12.5	3684.6 ± 1.09	30.56 ± 15.7	0.985
	25	2188.6 ± 1.47	35.67 ± 5.68	0.925
V15	0	4992.5 ± 3.76	33.27 ± 84.5	0.993
	1.56	4065.0 ± 4.63	32.06 ± 73.2	0..993
	3.13	3713.9 ± 7.54	37.89 ± 72.8	0.986
	6.25	3053.4 ± 8.11	42.01 ± 39.6	0.989

	12.5	1781.9 ± 22.1	42.90 ± 37.9	0.970
	25	604.7 ± 104.3	42.52 ± 37.0	0.877

5.3.2.2.V6 and V15 did not exhibit cell toxicity at as high as 50 µM concentration

We next assessed the cell toxicity of the compound V6 and V15 using MMT assay, given that potential tracers must be non-toxic compounds. We performed cellular toxicity study in the human neuroblastoma cell line, SH-SY5Y cells using MTT assay. The compounds were evaluated at two different concentrations 10 µM and 50 µM. The data, expressed as percent cell viability indicated that V6 and V15 had no toxic effect on the viability of the cells (**Figure 5.5**). Treatments were performed for 24 h. The percentages cell viability for V6 at 10 µM and 50 µM concentrations were 104.9±14.3% and 107.8%±6.5% respectively. The corresponding values for compound V15 at 10 and 50 µM concentrations were 102.0% ± 6.8% and 95.0% ± 11.3%, respectively. Furthermore, the morphological changes of the SH-SY5Y cells were observed under the inverted light microscope (**Figure 5.6**).

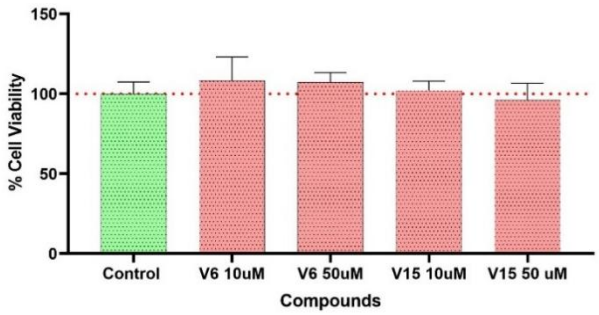

Figure 5.5. Cellular toxicity analyses for V6 and V15 using the human neuroblastoma cell line, SH-SY5Y cells. The analyses were done using MTT cell viability test. The cells were exposed for 24 hours to the 10 and 50 µM final concentrations of the compounds. Data are expressed as % mean values ± SD of 6 readings. Viability of the vehicle treated control cells were considered as 100%.

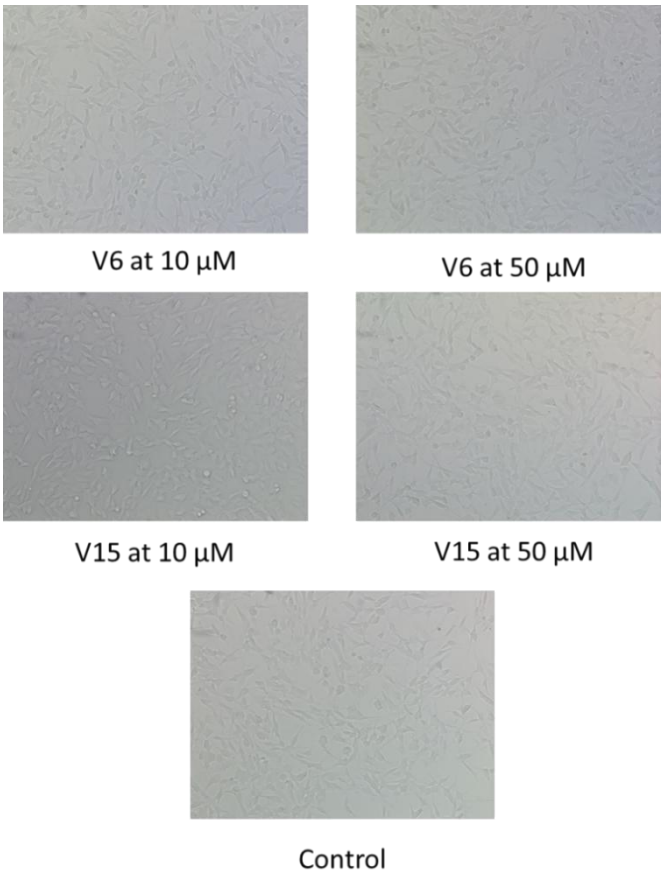

Figure 5.6. Morphological changes of SH-SY5Y cells as observed under an inverted light microscope (Nikon ECLIPSE TE300, 20× magnification).

5.3.3. Hit compounds V6 and V15 interacts well with the binding pocket of ChAT

ChAT protein is responsible for the biosynthesis of acetylcholine from choline by utilizing acetyl-coenzyme A (Acetyl-CoA) as the source of acetyl moiety. Choline and Acetyl-CoA enter from the opposite entrance sites of the catalytic tunnel of ChAT. The catalytic domain lies thereby between these two substrate binding sites within a narrow tunnel that extends across the enzyme. Then, the hydroxyl group of the choline moiety is activated by interaction with the HIS324 in the catalytic domain, and attacks the carbonyl carbon of the Acetyl-CoA thioester. Thus, HIS324 is essential for the catalytic function of ChAT (26). Nonetheless, several other amnio acid residues are present in the binding pocket viz. TYR552, ASP390, SER221, ARG403, TRP325, and GLY280, which also contribute significantly to the overall activity of ChAT.

Table. 5.4. Comparison of the docking scores from virtual screening and re-docking along with the MM/GBSA scores for the top 46 hits.

Sr. No.	Compound ID	Vina Docking Scores (kcal/mol)	Glide Docking Scores (kcal/mol)	MM/GBSA Scores (kcal/mol)
V1	STK214797	-10.5	-7.814	-43.68
V2	STK388849	-11.2	-7.795	-55.07
V3	STK895919	-10.7	-8.483	-63.7
V4	STL083128	-10.7	-7.622	-49.68
V5	STL108088	-10.5	-7.503	-53.73
V6	**STK161404**	**-10.6**	**-7.979**	**-66.93**
V7	STK175247	-10.6	-7.448	-62.77
V8	STK170827	-10.6	-7.676	-59.5
V9	STK219072	-10.7	-7.381	-46.74
V10	STK223530	-10.6	-7.617	-44.6
V11	STK156227	-10.5	-8.044	-54.99
V12	STK299795	-10.5	-7.728	-47.1
V13	STK094615	-10.7	-8.933	-65.14
V14	STL300279	-10.9	-7.489	-51.37
V15	**STK306932**	**-10.7**	**-7.533**	**-44.63**
V16	STK420897	-11.2	-7.627	-53.18
V17	STK643610	-10.6	-8.23	-50.55
V18	STK640056	-10.5	-7.643	-47.7
V19	STK690288	-10.6	-7.73	-52.3
V20	STL009303	-10.6	-8.756	-59.89
V21	STL247594	-10.9	-9.72	-51.18
V22	STL423291	-10.7	-8.166	-43.68
V23	STL518544	-10.7	-7.399	-51.78
V24	STL534544	-10.5	-8.86	-47.83
V25	STL537500	-10.5	-7.851	-58.67
V26	STL569268	-11.3	-7.561	-46.06
V27	STL316461	-10.5	-8.631	-45.42
V28	STL536828	-10.6	-7.647	-44.89
V29	STL520058	-10.6	-7.681	-49.37
V30	STL530439	-10.7	-7.561	-50.55
V31	STK806261	-10.6	-7.713	-51.67

V32	STK642171	-10.5	-7.542	-48.19
V33	STK607320	-11.1	-7.467	-45.25
V34	STK622314	-10.7	-7.406	-44.76
V35	STK631121	-10.7	-8.031	-44.46
V36	STK636132	-10.8	-8.939	-52.49
V37	STL464257	-10.7	-7.665	-54.59
V38	STL160294	-10.5	-8.099	-44.38
V39	STL009364	-10.5	-8.925	-46.61
V40	STK070091	-10.9	-7.757	-50.32
V41	STK494547	-10.5	-7.61	-51.94
V42	STK432350	-10.8	-7.604	-47.49
V43	STK084803	-10.7	-7.387	-56.09
V44	STK079698	-10.5	-8.992	-68.07
V45	STK055077	-10.6	-7.919	-52.53
V46	STK026652	-10.6	-7.467	-44.61

We performed and for comparison presented the docking scores obtained from the virtual screening and the Glide re-docking with the MM/GBSA scores (**Table 5.4**). Our analyses indicated that V6, with a Glide binding score of -7.979 kcal/mol, interacted through π-π stacking with HID324 through its furan ring (**Figure 5.7A**). Additionally, the carboxylic acid group of its chlorobenzene ring and the keto group of its imidazolidine ring formed two distinct hydrogen bonds with MET84 and SER438, respectively. We performed similar analyses on V15, which displayed an overall binding score of -7.533 kcal/mol, but a K_i value (4.4μM) that is approximately trice smaller than K_i of V6 (11 μM). Interestingly, we found that V15 formed four hydrogen bonds with the target protein, one with the crucial catalytic amino acid residue, i.e., HIS324 and the rest with SER540, SER96 and ASN88 amino acid residues owing to its amide and tetrazoline moieties (**Figure 5.7B**). Thereby, these could explain the higher potency of V15 compared to V6 as it can be deducted from a comparison of their K_i values.

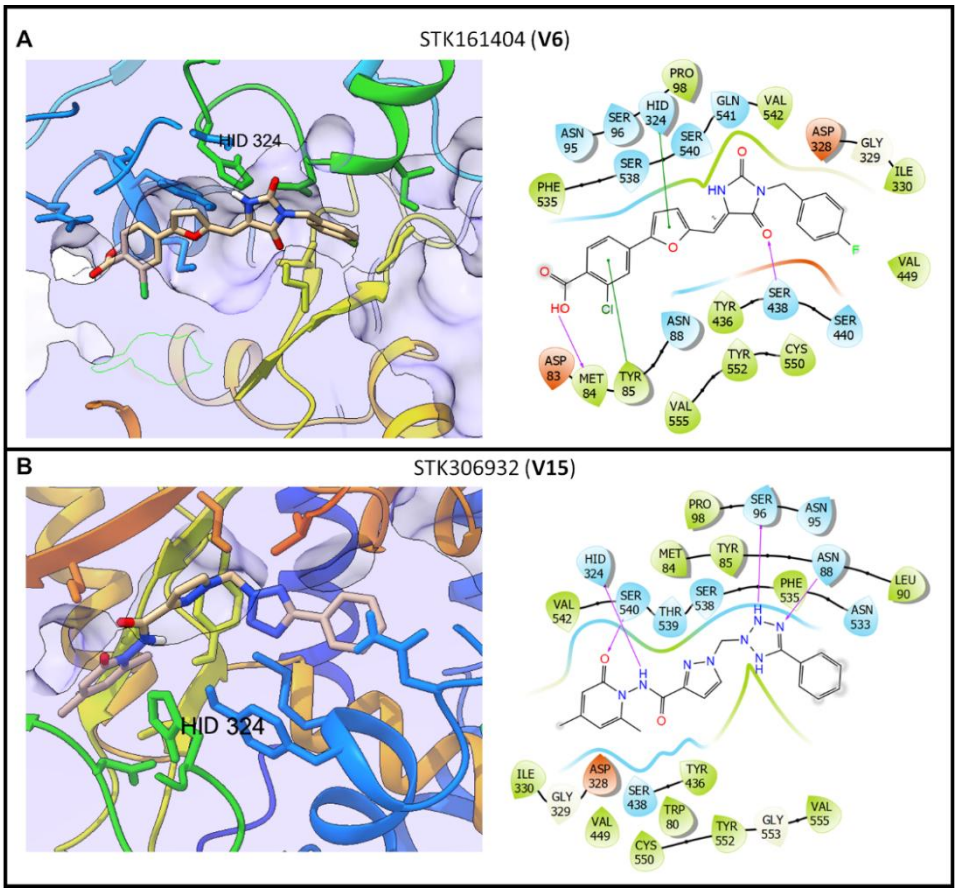

Figure 5.7. 3D and 2D docking interaction diagram for the top performing compounds V6 and V15. STK161404 and STK306932 are the catalogue numbers of these two compounds in the VitasM library.

5.3.4. Molecular Dynamics Simulation

Next, we conducted MD simulations on V6 and V15 to get insight into their dynamic interactions the ChAT protein, formation of complexes with the enzyme, the structural changes that might occur and the overall stability of the system with respect to time. The initial starting structure were taken from the docking results as an input for the MD simulations.

We first evaluated the RMSD for the ChAT protein complexed with the compound V6 and V15 in the simulation (**Figure 5.8A**), where the green and blue line represents the ChAT protein when complexed with the compound V6 and V15, respectively. The protein RMSD value started at around 0.15 nm for both complexes. It reached the equilibrium state within the first 10 ns, and remained stable throughout the simulation without any abrupt changes in the RMSD.

For the ChAT protein complexed with V6, the RMSD values ranged between 0.15 to 0.28 nm, and the values for the ChAT protein complexed with V15 (**Figure 5.8A**), was between 0.15 to 0.3 nm, a lower value with very narrow fluctuations indicates a robust complex system formation with the ligands during the simulation. Likewise, we evaluated the ligand RMSD value for V6 and V15 (**Figure 5.8B**). The RMSD value ranged 0.15 to 0.5 nm for V6 and 0.2 to 0.35 nm for V15, indicating good range of flexibility of the ligands in the binding pocket of the ChAT.

Next, we evaluated the simulated system for its RoG value (**Figure 5.8C**). ChAT_V6 and ChAT_V15 complexes displayed RoG values between 2.52 to 2.57 nm and 2.53 to 2.55 nm, respectively. Both complexes exhibited minor RoG fluctuations, suggesting that the overall size and shape of the complexes remained consistent throughout the simulation indicating good stability of the formed complex.

We then evaluated the system for its RMSF. The RMSF of the protein and the ligands were evaluated separately for fluctuations and flexibility. The RMSF values ranges between 0.1 to 1.2 nm for both ChAT_V6 complex, (**Figure 5.8D**) and ChAT_V15 complex (**Figure 5.8E**). The graphs illustrate a sharp peak for the N-terminus (residue ~0), indicating high flexibility at this part of the protein sequence, most likely due to a high exposure of the N-terminal surface with the solvent. Although the overall RMSF values landscape indicated that in general most of the ChAT protein exhibited low flexibility, we found high movement in certain regions in the enzyme´s binding cavity. RMSF analysis of the ligands (**Figure 5.8F**) showed that RMSF values ranged 0.06 to 0.4 nm for V6 and 0.04 to 0.25 nm for V15, indicating high flexibility that is necessary for forming complex with a target protein.

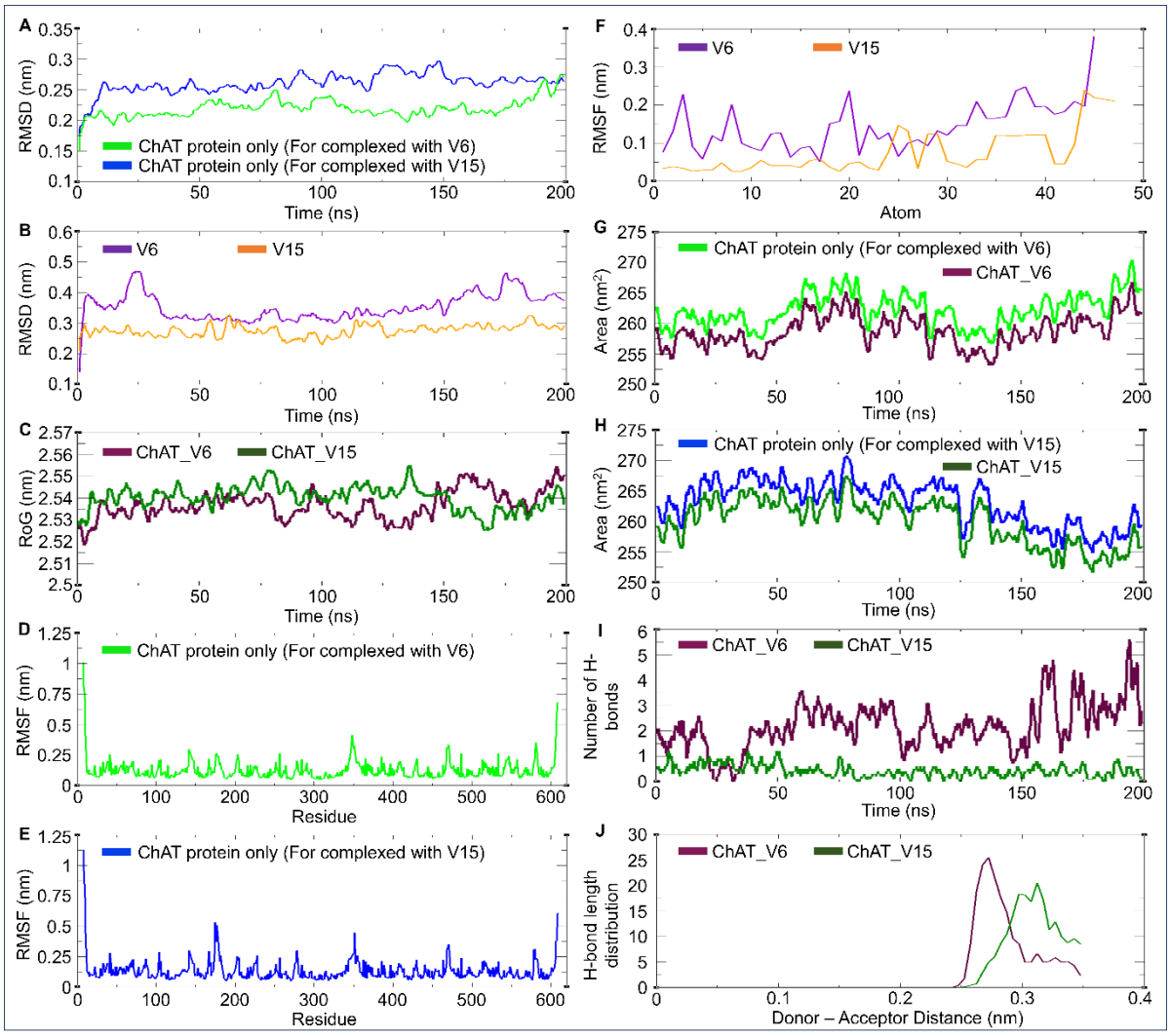

Figure 5.8. Comparative analysis for the 200 ns simulated MD trajectories A) RMSD plots for the ChAT protein (PDB ID: 2FY3) during formation of a complex with V6 (represented in green) and formation with V15 (represented in blue). B) RMSD plot for V6 (violet) and V15 (orange) during the simulation. C) RoG plot for ChAT_V6 (maroon) and ChAT_V15 complexes (deep green). D) RMSF landscape for ChAT protein during its complex formation with V6 throughout the simulation. E) The corresponding RMSF landscape for ChAT protein during its complex formation with V15. F) Represents the RMSF plot V6 (purple) and V15 (orange) during their complex formation with ChAT protein. G) The changes in SASA values of the ChAT_V6 complex (maroon) in comparison to the ChAT protein alone (green). H) The changes in SASA values of the ChAT_V15 complex (deep green) in comparison to the protein

ChAT (blue). I) shows the average numbers of H-bond formed within the ChAT_V6 (maroon) and ChAT_V15 (deep green) complexes J) Illustrate the average distance maintained by the formed H-bonds. It shows that distance was around the optimal value of 0.3 nm.

We also performed solvent accessible surface area analysis for the system under investigation. We wanted to see how the SASA pattern for the ChAT protein complexed with V6 (**Figure 5.8G**) differs compared to the pattern with ChAT protein alone, for instance how the SASA of the hydrophobic core of ChAT protein is changed upon formation of complex with the compounds. We found that the SASA for ChAT protein was higher (ranging 257 to 272 nm^2) compared to the ChAT_V6 complex (ranging 253 to 267 nm^2). This may suggest that the interaction with V6 stabilized the ChAT protein, leading to a slightly reduced and more stable SASA. A similar change in SASA levels was observed for the ChAT_V15 complex vs free ChAT protein (**Figure 5.8H**). For V15, the SASA level for ChAT protein alone ranged 255 to 270 nm^2 which is higher than the SASA level for the ChAT_V15 complex (252 to 267 nm^2). Thus, both compounds V6 and V15 stabilized the ChAT protein upon the complex formation.

Next, we analyzed the number of HBN for the system (**Figure 5.8I**), for the ChAT_V6 complex maintained 1-5 number of H-bonds over the time of simulation which is ideal. However, the ChAT_V15 complex maintained in average only one H-bond during the simulation time. Nonetheless, the distribution of hydrogen bond lengths was similar for both the ChAT_V6 complex (~0.29nm) and for the ChAT_V15 complex (0.3 nm), which both are within the ideal range of H-bond formation (**Figure 5.8J**).

Essential dynamics also known as principal component analysis was performed for the simulated the complexes. The PCA plots for V6 and V15 were prepared using the eigenvalues for the eigenvector index for the ChAT_V6 complex (**Figure 5.9A**) and ChAT_V15 (**Figure 5.9B**). The illustrated data shows that the contribution of the eigenvalues decrease rapidly from the first to the second eigenvector, and the decline continue for the subsequent eigenvectors.

This indicates that the first few principal components (particularly the first two PCs), account most significantly for the system's dynamics of the complexes. Therefore, the first two principal components were used for further analyses (**Figure 5.9C**). The ChAT_V6 and ChAT_V15 complexes both displays similar essential dynamics since the data points form distinct widespread clusters. This indicates that the conformational transitions were happening during the 200 ns MD simulation.

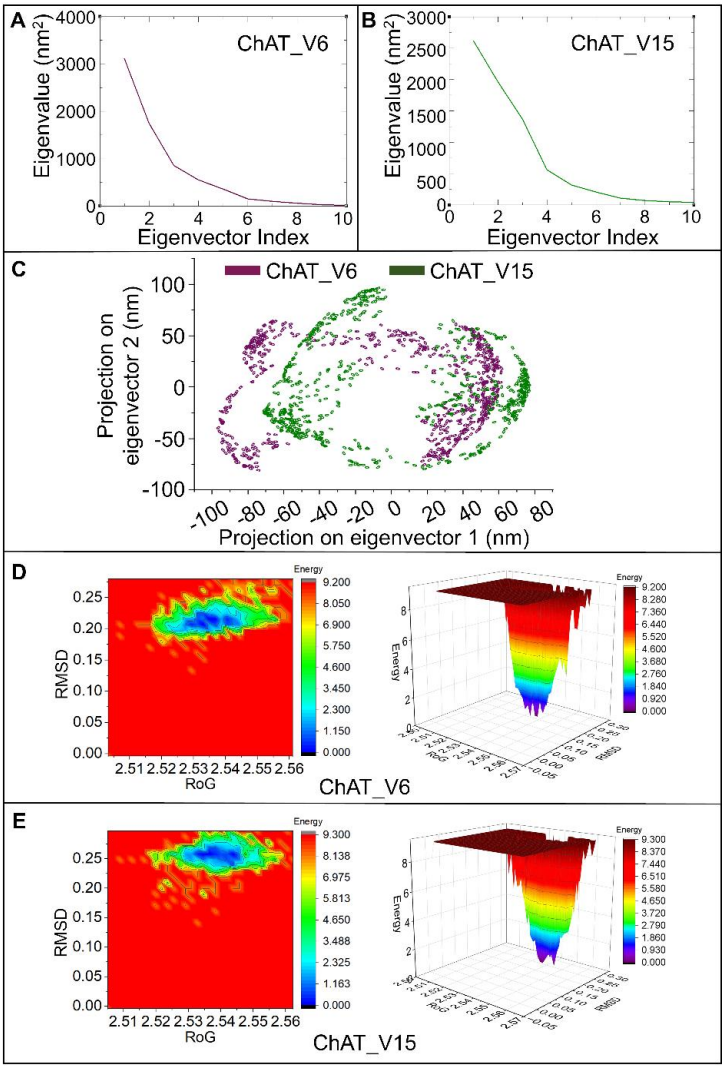

Figure 5.9. PCA and FEL analysis of the simulated systems. A) Eigenvalue calculation for the first 10 principal components for ChAT_V6. The result indicates that the first two principal components eigenvector accounts for most of the motions of the system. B) the corresponding

eigenvalue calculation for the first 10 principal components for ChAT_V15 complex, showing that also here the first two principal components eigenvector accounts for most of the motions of the system. C) PCA plot for the first two PCs for the simulated systems ChAT_V6 (maroon) and ChAT_V15 (deep green); D-E) The 2D and 3D plot representations of FEL analysis for ChAT_V6 and ChAT_V15, respectively.

Finally, we prepared the 3D FEL plot for the ChAT_V6 complex together with its 2D contour plot (**Figure 5.9D**). The 2D plot shows a distinct centralized low energy region (blue colour), which is displayed a sharp narrow funnel-shaped gorge in the 3D plot. The corresponding FEL analysis for the ChAT_V15 complex was essentially similar to that of ChAT_V6 complex. The findings are summarized as the 2D and 3D plots, shown in **Figure 5.9E**. Overall, the results indicates that both systems could form stable conformational arrangement and an energy minima conformation.

5.3.5. Similarity Index Analysis

Next, we performed Similarity Index Analysis, which is one of the most important aspects of such in silico virtual screening protocol. This is in simple term an estimation of chemical novelty of the identified compounds in comparison to the previously reported molecules. Thereby, giving rise to a completely new hit compound with better bioactivities and ideal physicochemical properties. The Tanimoto algorithm is a popular method to identify similarity between different compounds (27). It relies on a fingerprint-based representation, where each individual molecule is encoded to a series of bits that denotes the presence (1) or absence (0) of specific fragments within the chemical structure. We calculated three different molecular fingerprints (Morgan, atom pair, and MACCS), each of which offers unique advantages. The Morgan fingerprints are based on the circular neighborhoods of atoms, providing detailed and customizable structural information, ideal for in-depth molecular similarity searches. Atom Pair fingerprint approach calculates the pairs of atoms and their topological distance with each other,

capturing medium range structural information in the molecule. It is useful for representation of the molecular shape, making it ideal for shape-based similarity searches. MACCS fingerprint predefines set of structural keys, representing the presence or absence of certain features (like presence of a particular functional group in the molecule). It is ideal for quick similarity search and substructure screening. These measures are given as Tanimoto coefficient, which ranges between 0 and 1 represented in X-axis. A larger coefficient reflects a higher similarity between the compounds, while a lower coefficient indicates more dissimilarity

Compound V6 (STK161404) shows Tanimoto similarity of 0.15 using Morgan fingerprint with the earlier reported compound STK927381, while using Atom Pair fingerprint and MACCS fingerprint it showed a Tanimoto similarity of 0.42 and 0.44 respectively with the earlier reported compound STK111399. Likewise, the compound V15 (STK306932) shows Tanimoto similarity in Morgan fingerprint of 0.17 with the known ChAT inhibitor, STK111399, while using Atom Pair fingerprint and MACCS fingerprint it showed a Tanimoto similarity of 0.46 and 0.54 with Ilaprazole (earlier reported ChAT inhibitor) (**Figure 5.10**). The findings indicated that our hit compounds V6 and V15 are novel and structurally diverse moiety as it shows very less similarity to previously reported inhibitors of ChAT obtained from CHEMBL and compounds reported by our lab previously.

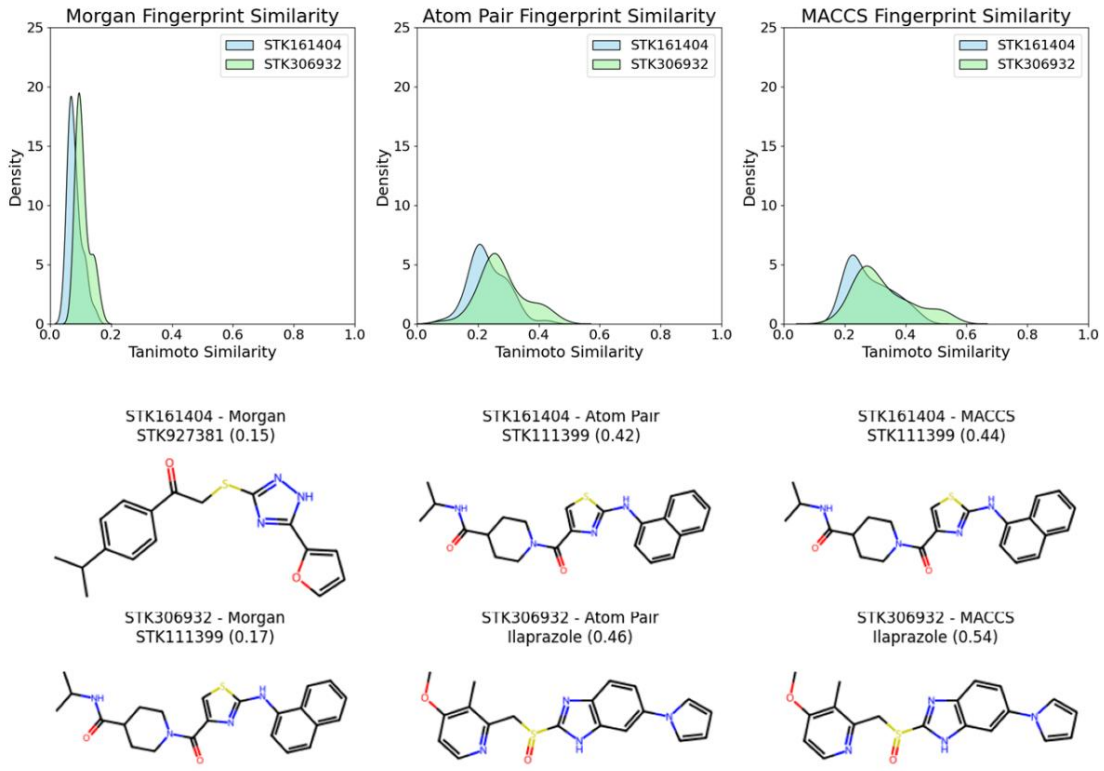

Figure 5.10. Histograms of structural similarity shown as Tanimoto coefficient of the hit compounds STK161404 (V6) and STK306932 (V15) against reported human ChAT inhibitors. Active compounds against human ChAT were obtained from ChEMBL (ID: CHEMBL4039) and compared to the two identified hit compounds using Morgan, AtomPair and MACCS fingerprints using RDKit.

5.3.6. Solubility study

Solubility is one of the crucial parameters in the context of drug discovery, as it is a necessary physicochemical parameter for achieving the desired drug concentration in systemic circulation to exert pharmacological effect (28). Aqueous solubility is directly related to the absorption and bioavailability of the drug administered through oral route as well as a challenging factor to be considered for intravenous (i.v.) dosing, ultimately affecting drug development time and cost. (29) Given our ultimate goal is to develop the identified compounds as in vivo biomarkers for ChAT-containing targets in the brain, an optimal balance between the hydrophilicity and lipophilicity will be the key to obtain good pharmacokinetic profiles. Calibration curve was

prepared beforehand (**Figure 5.11**) to quantify the kinetic solubility studies for the compound V6 and V15. It revealed that the solubility for V6 and V15 was 0.21 mg/ml and 0.17 mg/ml, respectively. This suggests that at pH 7.4, compound V6 may exhibit better aqueous solubility than V15. Percentage purity calculations were also carried out for the compounds at 100 µM concentrations, which are shown as chromatogram in (**Figure 5.12**). The purity was 96.94 % for V6 and 91.67 % for V15.

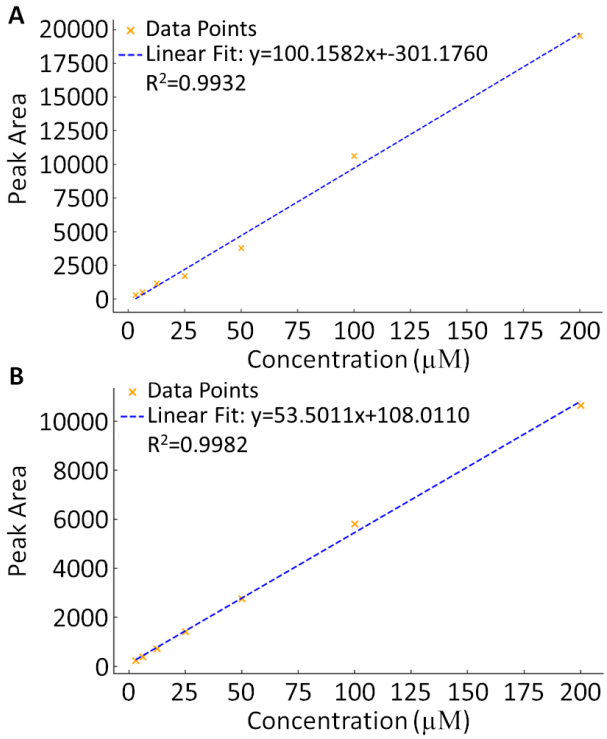

Figure. 5.11. HPLC calibration curve for the compounds using serial dilutions of 200 µM, 100 µM. 50 µM. 25 µM, 12.5 µM, 6.25 µM and 3.125 µM **A)** V6, R2 value was 0.9932; **B)** V15, R^2 value was 0.9982.

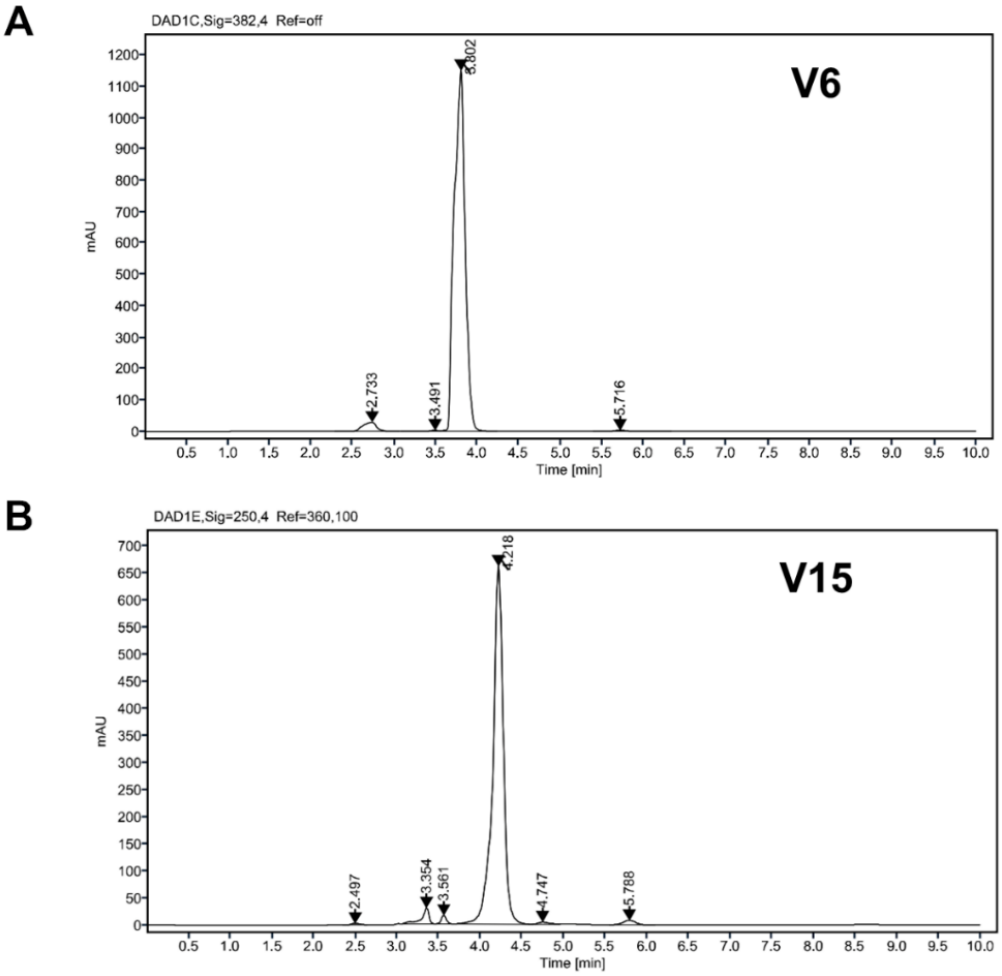

Figure. 5.12. Single injection HPLC chromatogram of hit compounds for percentage purity calculation. A) V6, Solvent system used Acetonitrile = 90%: Water = 10%, Flow rate was set to 0.4 ml/min, Absorbance was recorded at 382 nm; **B)** V15 Solvent system used Acetonitrile = 75%: Water = 25%, Flow rate was set to 0.4 ml/min, Absorbance was recorded at 250 nm.

5.4. Material Methods

5.4.1. Virtual screening protocol

5.4.1.1. Protein structure preparation

The 3D X-ray crystallographic structure of the target protein hChAT in complex with choline was obtained from the Protein Data Bank (PDB) (30) (PDB ID: 2FY3), (26) having a resolution of 2.27 Å. There are two primary binding sites in ChAT, CoA binding site and choline binding site. In between these two binding sites lies the catalytic domain which consist of amino acid

residue HIS324 which is responsible for the transfer of the acetyl group from Coenzyme-A to choline (26, 31). The protein was prepared by using AutoDock Tools (ADT) where all the unwanted water and ion molecules were removed, followed by the addition of the polar hydrogen bonds, then the AD4 bond was assigned and finally Kollman charges were added to the protein and saved as PDBQT format (32).

5.4.1.2. VitasM screening library acquisition and preparation

We download the VitasM laboratory database consisting of 1.4 million small molecules (structure data file; SDF) from https://vitasmlab.biz/. The library was preliminary filtered for molecules with optimal physicochemical parameters like molecular weight (100 to 500 Da), number of hydrogen bond donors (1 to 5), number of hydrogen bond acceptors (1 to 10), polar surface area (20 to 90) ClogP (-4 to 5), Number of rings (1 to 6), Number of rotatable bonds (1 to 10). Finally, PAINS filter was also applied in order to remove any compounds that may result in false positive outcomes (33, 34). On screening the library size was reduced to ~8,00,000. The library was finally subjected to energy minimization using MMFF94 force field and was converted to PDBQT format for virtual screening using the Open Babel (35).

5.4.1.3. Virtual Screening

The structure based virtual screening protocol was carried out using Vina-MPI (22) on high performance computing facility 'Paramshivay' available at IITBHU, Varanasi. First the grid box was generated using ADT, where the choline bound to the ChAT structure in the co-crystallized PDB was taken as the centroid for the generation of the grid box and was ensured that all the necessary residues of the active cavity were inside the box including the catalytic residue HIS324. The gridbox dimensions were set to 28 X 28 X 28 Å and the X, Y and Z coordinates were set to 6.528, 3.667 and 66.944 respectively. Exhaustiveness was set to 8 (36) and finally, the virtual screening protocol was carried out generating 9 poses for each compound. The first pose was selected for the docking scores based on which further decisions

were made.

5.4.1.4. Post screening rescoring and MM/GBSA analysis

The top scoring 5958 molecules from the Virtual screening protocol were selected for Xtra precision docking using Glide available on Schrodinger maestro (37). Where the protein was prepared using the protein preparation wizard available on glide, followed by the grid box preparation wizard where the Choline was selected as the centroid for the grid box preparation. The top scoring hits were prepared using the ligand preparation wizard and finally docked on ChAT using the Ligand docking wizard with Xtra precision (XP) mode. The tops performing 250 compounds were then subjected to the MMGBSA free energy calculation using Maestro (38).

5.4.2. Production and purification of recombinant human ChAT protein

Recombinant human ChAT protein was produced and purified by the Protein Science Facility (PSF) at Karolinska Institute/SciLifeLab (http://ki.se/psf), as described before (19). The purity of protein was determined using sodium dodecyl sulfate polyacrylamide gel (SDS-PAGE) stained with Coomassie blue dye. The total protein concentration was measured using BioRad DC protein Assay (BioRad). The storage buffer for the protein was 20 mM HEPES buffer, pH 7.5, containing 300 mM NaCl, 0.5 mM TCEP. The protein was diluted in the storage buffer to a concentration of 212 μg/mL. The diluted enzyme solution was then aliquoted (10μL/tube), frozen on dry ice, and stored at -20°C.

5.4.2.1. In vitro fluorometric ChAT activity inhibition assay

To validate our findings from the virtual screening the top 46 hit molecules were purchased from the VitasM library and were subjected to *in-vitro* ChAT activity inhibition assay using our in-house developed high throughput fluorometric method, utilising recombinant human ChAT (rChAT) protein. (21) The required reagents choline chloride, acetyl coenzyme-A (ACoA, A2181) and 7-Diethylamino-3-(4-maleimidophenyl)-4-methylcoumarin (CPM) for carrying

out the study were purchased from Sigma-Aldrich (St. Louis, MO, USA).

The ChAT assay was run in 384-well plates (Greiner Bio-One Item-No. 781209). The dilution buffer was 20mM HEPES, pH 7.4 (containing 150 mM NaCl, 1.0 mM EDTA, 0.05% (v/v) Triton X-100). First, 20 µL/well of a 600µM choline chloride solution (final concentration, C_f, 150 µM), and then 20 µL/well of a 0.212µg/ml of the recombinant ChAT (C_f = 0.053µg/mL) was added. Thereafter, 20µL/well of 400µM of different hit compounds were added to the wells, and incubated for ~30 minutes at room temperature under gentle orbital shaking (200rpm). Finally, the reaction was started by adding 20µL of a cocktail-A [containing 54µM ACoA (C_f = 13.3 µM) and 60 µM CPM (C_f = 15 µM)] was to each well. Immediately after adding the cocktail-A, the changes in fluorescence were monitored continuously at 3 minutes intervals for 30 minutes using a microplate spectrophotometer reader (Infinite M1000, Tecan). The excitation and emission wavelengths were 390 nm and 479 nm, respectively. Each compound was applied in six replicates. On each 384-wells plate, several enzyme wells without any hit compounds but the vehicle were also included to serve as reference enzyme control wells. The vehicle was the compound dilution buffer containing the same amount of DMSO as the compound's wells. Negative controls (or blanks) were wells without enzyme. The total volume in all wells were 80µL. The percentage inhibition for each compound was calculated based on the enzyme control value as a reference (100% activity). Based on the initial screening we selected the two most potent compounds that inhibited ChAT selectively for the enzyme inhibition kinetic studies.

5.4.2.2. In vitro colorimetric AChE and BChE activity inhibition assay

An in-house high throughput assay for the enzymatic activity of BChE and AChE was designed using a modified version of Ellman's colorimetric assay. The reagents, butyrylthiocholine iodide (BTC), acetylthiocholine iodide (ATC), and 5,5′-dithiobis (2-nitrobenzoic acid) (DTNB), were purchased from Sigma-Aldrich (St. Louis, MO, USA). The buffer system for

AChE and BChE assays was sodium/potassium phosphate buffer (50mM, pH 7.4).

Briefly, for screening of compounds against BChE, 20 µL/well of a 1:100 diluted solution of a pooled human plasma (final dilution 1/400) was added to the wells of a 384 well plate (a flatbottom transparent plate). For screening against AChE, 20 µL/well of a 1:768 diluted (C_f = 3.5 ng/mL) solution purified recombinant human AChE protein (Sigma, Cat no. C1682) was used. Then 20 µL/wells of a 400µM hit compounds solution (C_f = 100µM) was added to the assigned wells (six replicates/compound), followed by adding 20µL/well of a 1.6 mM freshly prepared solution of DTNB (C_f = 0,4 mM) to all wells. The plate was incubated at RT for ~30 min. On each 384-wells plate, several enzyme wells without any hit compounds but the vehicle were also included to serve as reference enzyme control wells. The vehicle contained the same amount of DMSO as the compound's wells. Negative controls (or blanks) were wells without enzyme. Lastly, 20 µL of a 4.0 mM BTC solution (C_f = 1 mM) or a 2.0 mM ATC (C_f = 0.5 mM) was added to each well, and the changes in absorbance were continuously monitored at 412 nm wavelength for 10 min with 1 min interval, using a microplate spectrophotometer reader (Infinite M1000, Tecan). The rate of the enzyme activity was determined from the linear part of the kinetic reaction curves as ΔOD/time. The total volume in all wells were 80µL. The percentage inhibition for each compound was calculated based on the enzyme control value as a reference (100% activity).

5.4.2.3. Enzyme inhibition kinetics for determination of K_i, IC_{50}, and mode of action of hits compounds

Likewise, an identical protocol as inhibition assay was performed, a 2-fold dilution series of the compound is dispensed to 384 well plate, starting with a stock concentration of 50 mM. The compound is then diluted to five different concentrations of dilution series ranging from 100 to 1.56 µM for the top selected compound V6 and V15. Followed by preparing and adding a 2-fold dilution series of choline to each well. The final concentrations of choline range from 320

µM to 0 µM. ChAT enzyme solution is added to each well resulting in a final concentration of 0.053 µg/mL in each well. The 384 well plate is incubated at room temperature with 200 rpm orbital shaking for 30 minutes. The spectrophotometer is set up for read fluorescence intensity reading at 3-minute intervals. The excitation wavelength is set at 390 nm and the emission is measured at 479 nm. Finally, a 4-fold fluorescent detection reagent solution, which is prepared by mixing dilution buffer, 1 mM ACoA, and CPM stock solution was added (20 µL/well), resulting in a final concentration of 13.33 µM, 60 µM, and 15 µM, respectively. The rate of enzyme activity (RFU/hr/53ng rChAT) was calculated and processed using the GraphPad Prism 7 analysis software(39). The inhibitory constant (K_i) values were determined from the dose-response curve along with the half-maximal inhibitory concentration (IC_{50}) calculated by plotting the percentage enzyme activity vs. the log of the compounds concentrations and fitting it with the nonlinear regression enzyme kinetics-inhibition function. The Michaelis-Menten constant (K_m) and maximal velocity (V_{max}) values were also obtained from the substrate-velocity curve by fitting the data with non-linear regression Michaelis-Menten kinetic function. These values were then used for making the Lineweaver-Burk plot and was fitted using the linear regression function.

5.4.2.4. Cell viability assay

MTT assay was performed for the top performing compound V6 and V15 to determine the *in vitro* cellular toxicity (40). Human neuroblastoma SH-SY5Y cells (ATCC, CRL-2266) were cultured at 37°C in a humidified environment with 5% CO_2 in Dulbecco's Modified Eagle's medium (DMEM) with 10% fetal bovine serum (FBS) in 96-well plate to obtain 70–80% confluency. The cells were incubated with 10 µM and 50 µM compounds in sextuplicate for 24 h at 37 °C. Cells treated with 0.25% DMSO were used as controls. At the end of the treatment, 20 µL of MTT (5 mg/mL in Phosphate buffer saline pH 7.4) was added to each well and incubated for an additional 4 h at 37 °C. The media was then removed from the plate and 200

µL of DMSO was added to dissolve the violet formazan crystals. Finally, the absorbance was measured at 570 nm with a reference wavelength of 630 nm on CLARIOstar Plus microplate reader (BMG Labtech) with shaking before the reading. The percentage viability was calculated taking 0.25% DMSO control as 100 percent and represented as mean ± SD.

5.4.3. Molecular Dynamics simulation

Molecular dynamics simulation was performed for the two top performing hits with the help of GROMACS 2020 (41, 42) and CHARMM36M force field (43) was used. The redocked pose obtained from the Glide XP docking protocol was taken as the starting frame for the simulation. System preparation was performed as per the protocol mentioned in our previous article. Briefly, the complexes were solvated in a cubic box and TIP3 mode used as a water model for the system, with a 1.0 nm distance from each side of the complex and between the solvation box edges. 0.15 molar Na^+ and Cl^- ions was added to neutralize the system. The built system was then subjected to energy minimization by utilizing the steepest descent algorithm such that the maximum forces become less than 1000 kJ/mol/nm in order to obtain a decent starting structure for the simulation production run. Position restraints were set for the equilibration step by constant moles, volume and temperature in the canonical ensemble (NVT) and isothermal-isobaric ensemble (NPT), each for 2ns so as to prevent distortions that can result in blow up of the system during the production run due to the lack of stability. The system condition was kept at 310.15 K temperature applying the V-rescale temperature coupling and pressure was maintained at 1 bar using the Parrinello–Rahman pressure coupling with a coupling constant of 0.1 picosecond for the temperature setting and 2 picoseconds for the pressure setting. Particle mesh Ewald (PME) method was used to calculate the long-range electrostatic interactions and van der Waals interactions, the cut-off for short-range van der Waals was set to 1 nm (44). LINCS algorithm was used for setting constraints on the bonds and the time step was kept at 0.002 ps for the simulation run (45). Finally, a 200 ns production run was initiated under the

periodic boundary conditions. The obtained trajectories were further analyzed for its RMSD, RMSF, RoG, SASA, HBN, HBD, PCA and FEL.

5.4.4. Similarity Index Analysis

We calculated the structural diversity of the hit compounds V6 and V15 by comparing their Tanimoto similarity with already reported compounds obtained from ChEMBL database and literature, considering IC_{50} values as indicator of the compound potency. We extracted the unique molecular structures (SMILES strings) of these compounds and removed duplicates to ensure data integrity and generated molecular fingerprints (Morgan, atom pair, and MACCS) for both the database compounds and the hit compounds using RDKit (46). Using these fingerprints, we computed Tanimoto similarity scores to quantify the structural resemblance between each query compound and the database molecules (27). We visualized the calculated similarity scores using kernel density estimation plots, which provided insights into the distribution of similarity values across different fingerprint types (47).

5.4.5. Solubility and parentage purity assay

Solubility study was performed as reported earlier (48). Initially making a primary stock solution of 10 mM of each compound V6 and V15 in an organic solvent (DMSO), followed by taking 50 µL of the 10 mM DMSO stock and adding it to a 950 µL of 1 M phosphate buffer saline (PBS) with a pH of 7.4. The resultant solution was set for 1.5 hours of mixing. The resultant solution was centrifuged and filtered using 0.22 µm nylon syringe filter and was quantified using RP-HPLC method. Calibration curve was made for the compounds by taking 7 serial dilutions as follows, 200 µM, 100 µM. 50 µM. 25 µM, 12.5 µM, 6.25 µM and 3.125 µM, and the R^2 value for the compound V6 and V15 was found to be 0.9932 and 0.9982 respectively. The percentage purity calculations were carried out using the 100 µM sample concentrations, chromatograms are shown in (**Figure 5.11**). HPLC Instrument used: Agilent 2004, Method for V6: Solvent system used Acetonitrile = 90%: Water = 10% and for V15:

Solvent system used Acetonitrile = 75%: Water = 25%, Flow rate was set to 0.4 ml/min. Absorbance was recorded at 382 nm and 250 nm for compound V6 and V15 respectively. Sample volume for each injection was 20 µl, Column Specification: Poroshell 123, EC C18 4 µm, 4.6*150 mm.

5.5. Conclusion

With the urgency and importance for the need of novel biomarkers in the field of AD and ALS diagnostics, the present work focused on the discovery of novel ChAT ligands having potential to be further developed into radio-labelled marker compounds for in-vivo PET imaging for mapping the distribution and concentration of ChAT in CNS, PNS and ENS, as the ultimate indicator of the health and function of the cholinergic neuronal system. To access these objectives there are a need for novel ligand with high selectivity towards ChAT and optimum pharmacokinetic parameters along with good BBB permeability.

As was noted before, the few known classical inhibitors of ChAT lack the critical properties, such as selectivity and BBB permeability. Considering such limitations, our research group have previously identified and characterized three compounds from Asinex chemical database. These three compounds (B1, B4 and E1) behaved like mixed-competitive inhibitors of ChAT, with K_i values of 9.4 µM, 16.5µM and 25.4 µM, respectively (21). In another study we assessed the FDA chemical database over approved drugs and reported for the first time an unprecedented mechanistic link between use of proton pump inhibitors (PPI's) with incidence of dementia, through an unprecedented potent inhibitory effect on ChAT (19). Among the tested PPIs, omeprazole/esomeprazole, tenatoprazole and rabeprazole emerged to be the most potent ChAT inhibitors. The K_i values for these PPIs were determined to be between 160nM to as low as 18nM. The dominant mode of ChAT inhibition by these PPIs was non-competitive reversible type. Initial docking analyses revealed that the pyridine ring in the PPI's interact with the catalytic amino acid residue HIS324 in the catalytic tunnel of ChAT, potentially accounting for

the inhibition. However, the BBB permeability of PPI's is not well-known and the available literature indicates it to be about 10% of the concentration of the drug in circulation, (19) which might not be optimal for use as molecular probes of ChAT in the brain. Nonetheless, further studies are required scaffold exploration and SAR studies to further improve the affinity for ChAT and make other optimization required for developing molecular probes of ChAT with ideal pharmacological properties, for instance as PET tracers.

Here, in the present study, we report two additional novel scaffolds as a ligand of ChAT. To achieve this, we subjected a compound library of 1.4 million compounds from VitasM to various filters and structure-based virtual screening protocol for hits with novel scaffold, high selectivity and BBB permeability based on various optimal physicochemical parameters and PAINS filter. This resulted in 769609 hit compounds that were further subjected to a docking-based virtual screening, yielding 5958 potential hits with good docking scores. These were then re-docked using Glide for cross platform validity of the docking results, and the final top scored hits were then subjected to MM/GBSA rescoring. This resulted to 46 top hit compounds for in-vitro screening. The compounds were purchased and were screened in vitro against human ChAT protein using our in-house high-throughput non-radiometric fluorescence assay. To assess their selectivity the hits were also screened against the potential anti-target enzymes, human AChE and BChE. The top two compounds, V6 and V15, had an IC_{50} value in the low micromolar range, 21.7 µM and 9.4 µM, respectively. Compound V6 exhibited better kinetic solubility (0.21 mg/ml), as compared to V15, which had a solubility of 0.17 mg/ml. Both compounds V6 and V15 displayed no toxicity as was assessed by MTT assay, demonstrating ideal characteristics for potential diagnostic biomarkers.

Overall, by a combination of rigorous virtual screening and our high-throughput ChAT assay *in vitro* screening, we successfully identified two compounds, with high selectivity, low toxicity and good potency as ChAT inhibitors with structural diversity in comparison to previously

reported ChAT ligands.

5.6. References

1. Andrade-Guerrero J, Santiago-Balmaseda A, Jeronimo-Aguilar P, Vargas-Rodríguez I, Cadena-Suárez AR, Sánchez-Garibay C, et al. Alzheimer's disease: an updated overview of its genetics. International journal of molecular sciences. 2023;24(4):3754.
2. Theleritis CG, Siarkos KT, Politis AM. Unmet needs in pharmacological treatment of apathy in Alzheimer's disease: a systematic review. Frontiers in pharmacology. 2019;10:1108.
3. Melnikova I. Therapies for Alzheimer's disease. Nature Reviews Drug Discovery. 2007;6(5).
4. Moloney EB, de Winter F, Verhaagen J. ALS as a distal axonopathy: molecular mechanisms affecting neuromuscular junction stability in the presymptomatic stages of the disease. Frontiers in neuroscience. 2014;8:252.
5. Du X, Wang X, Geng M. Alzheimer's disease hypothesis and related therapies. Translational neurodegeneration. 2018;7:1-7.
6. Cheng K, Samimi R, Xie G, Shant J, Drachenberg C, Wade M, et al. Acetylcholine release by human colon cancer cells mediates autocrine stimulation of cell proliferation. American Journal of Physiology-Gastrointestinal and Liver Physiology. 2008;295(3):G591-G7.
7. Friedman JR, Richbart SD, Merritt JC, Brown KC, Nolan NA, Akers AT, et al. Acetylcholine signaling system in progression of lung cancers. Pharmacology & therapeutics. 2019;194:222-54.
8. Leifer BP. Early diagnosis of Alzheimer's disease: clinical and economic benefits. Journal of the American Geriatrics Society. 2003;51(5s2):S281-S8.
9. Mesulam MM. Cholinergic circuitry of the human nucleus basalis and its fate in Alzheimer's disease. Journal of Comparative Neurology. 2013;521(18):4124-44.
10. Mukaetova-Ladinska EB, Andras A, Milne J, Abdel-All Z, Borr I, Jaros E, et al. Synaptic proteins and choline acetyltransferase loss in visual cortex in dementia with Lewy bodies. Journal of Neuropathology & Experimental Neurology. 2013;72(1):53-60.
11. Yates C, Simpson J, Maloney A, Gordon A, Reid A. Alzheimer-like cholinergic deficiency in Down syndrome. The Lancet. 1980;316(8201):979.
12. Bohnen NI, Kaufer DI, Ivanco LS, Lopresti B, Koeppe RA, Davis JG, et al. Cortical cholinergic function is more severely affected in parkinsonian dementia than in Alzheimer disease: an in vivo positron emission tomographic study. Archives of neurology. 2003;60(12):1745-8.
13. Oda Y. Choline acetyltransferase: the structure, distribution and pathologic changes in the central nervous system. Pathology international. 1999;49(11):921-37.
14. Casas C, Herrando-Grabulosa M, Manzano R, Mancuso R, Osta R, Navarro X. Early presymptomatic cholinergic dysfunction in a murine model of amyotrophic lateral sclerosis. Brain and behavior. 2013;3(2):145-58.
15. Kato T, Inui Y, Nakamura A, Ito K. Brain fluorodeoxyglucose (FDG) PET in dementia. Ageing research reviews. 2016;30:73-84.
16. Matsuda H, Shigemoto Y, Sato N. Neuroimaging of Alzheimer's disease: focus on amyloid and tau PET. Japanese journal of radiology. 2019;37:735-49.
17. Soleimani-Meigooni DN, Iaccarino L, La Joie R, Baker S, Bourakova V, Boxer AL, et al. 18F-flortaucipir PET to autopsy comparisons in Alzheimer's disease and other neurodegenerative diseases. Brain. 2020;143(11):3477-94.

18. Rowley PA, Samsonov AA, Betthauser TJ, Pirasteh A, Johnson SC, Eisenmenger LB, editors. Amyloid and tau PET imaging of Alzheimer disease and other neurodegenerative conditions. Seminars in Ultrasound, CT and MRI; 2020: Elsevier.
19. Kumar R, Kumar A, Nordberg A, Långström B, Darreh-Shori T. Proton pump inhibitors act with unprecedented potencies as inhibitors of the acetylcholine biosynthesizing enzyme—a plausible missing link for their association with incidence of dementia. Alzheimer's & Dementia. 2020;16(7):1031-42.
20. Baidya AT, Das B, Devi B, Långström B, Ågren H, Darreh-Shori T, et al. Mechanistic insight into the inhibition of choline acetyltransferase by proton pump inhibitors. ACS Chemical Neuroscience. 2023;14(4):749-65.
21. Kumar R, Kumar A, Långström B, Darreh-Shori T. Discovery of novel choline acetyltransferase inhibitors using structure-based virtual screening. Scientific reports. 2017;7(1):16287.
22. Ellingson SR, Smith JC, Baudry J. VinaMPI: Facilitating multiple receptor high-throughput virtual docking on high-performance computers. Wiley Online Library; 2013.
23. Zhang B, Li H, Yu K, Jin Z. Molecular docking-based computational platform for high-throughput virtual screening. CCF Transactions on High Performance Computing. 2022:1-12.
24. Neves BJ, Mottin M, Moreira-Filho JT, de Paula Sousa BK, Mendonca SS, Andrade CH. Best practices for docking-based virtual screening. Molecular docking for computer-aided drug design: Elsevier; 2021. p. 75-98.
25. Hosseini M, Chen W, Xiao D, Wang C. Computational molecular docking and virtual screening revealed promising SARS-CoV-2 drugs. Precision clinical medicine. 2021;4(1):1-16.
26. Kim A-R, Rylett RJ, Shilton BH. Substrate binding and catalytic mechanism of human choline acetyltransferase. Biochemistry. 2006;45(49):14621-31.
27. Bajusz D, Rácz A, Héberger K. Why is Tanimoto index an appropriate choice for fingerprint-based similarity calculations? Journal of cheminformatics. 2015;7:1-13.
28. Vemula VR, Lagishetty V, Lingala S. Solubility enhancement techniques. International journal of pharmaceutical sciences review and research. 2010;5(1):41-51.
29. Di L, Kerns EH. Drug-like properties: concepts, structure design and methods from ADME to toxicity optimization: Academic press; 2015.
30. Bank PD. Protein data bank. Nature New Biol. 1971;233(223):10-1038.
31. Govindasamy L, Pedersen B, Lian W, Kukar T, Gu Y, Jin S, et al. Structural insights and functional implications of choline acetyltransferase. Journal of structural biology. 2004;148(2):226-35.
32. Huey R, Morris GM, Forli S. Using AutoDock 4 and AutoDock vina with AutoDockTools: a tutorial. The Scripps Research Institute Molecular Graphics Laboratory. 2012;10550(92037):1000.
33. Senger MR, Fraga CA, Dantas RF, Silva Jr FP. Filtering promiscuous compounds in early drug discovery: is it a good idea? Drug Discovery Today. 2016;21(6):868-72.
34. Chakravorty SJ, Chan J, Greenwood MN, Popa-Burke I, Remlinger KS, Pickett SD, et al. Nuisance compounds, PAINS filters, and dark chemical matter in the GSK HTS collection. SLAS Discovery: Advancing Life Sciences R&D. 2018;23(6):532-45.
35. O'Boyle NM, Banck M, James CA, Morley C, Vandermeersch T, Hutchison GR. Open Babel: An open chemical toolbox. Journal of cheminformatics. 2011;3:1-14.
36. Agarwal R, Smith JC. Speed vs accuracy: effect on ligand pose accuracy of varying box size and exhaustiveness in AutoDock vina. Molecular Informatics. 2023;42(2):2200188.
37. Maestro S. Maestro. Schrödinger, LLC, New York, NY. 2020;2020:682.
38. Genheden S, Ryde U. The MM/PBSA and MM/GBSA methods to estimate ligand-binding affinities. Expert opinion on drug discovery. 2015;10(5):449-61.

39. Swift ML. GraphPad prism, data analysis, and scientific graphing. Journal of chemical information and computer sciences. 1997;37(2):411-2.
40. Mosmann T. Rapid colorimetric assay for cellular growth and survival: application to proliferation and cytotoxicity assays. Journal of immunological methods. 1983;65(1-2):55-63.
41. Van Der Spoel D, Lindahl E, Hess B, Groenhof G, Mark AE, Berendsen HJ. GROMACS: fast, flexible, and free. Journal of computational chemistry. 2005;26(16):1701-18.
42. Abraham MJ, Murtola T, Schulz R, Páll S, Smith JC, Hess B, et al. GROMACS: High performance molecular simulations through multi-level parallelism from laptops to supercomputers. SoftwareX. 2015;1:19-25.
43. Huang J, Rauscher S, Nawrocki G, Ran T, Feig M, De Groot BL, et al. CHARMM36m: an improved force field for folded and intrinsically disordered proteins. Nature methods. 2017;14(1):71-3.
44. Cheatham TI, Miller J, Fox T, Darden T, Kollman P. Molecular dynamics simulations on solvated biomolecular systems: the particle mesh Ewald method leads to stable trajectories of DNA, RNA, and proteins. Journal of the American Chemical Society. 1995;117(14):4193-4.
45. Hess B, Bekker H, Berendsen HJ, Fraaije JG. LINCS: a linear constraint solver for molecular simulations. Journal of computational chemistry. 1997;18(12):1463-72.
46. Yoshimori A. Prediction of molecular properties using molecular topographic map. Molecules. 2021;26(15):4475.
47. Ralaivola L, Swamidass SJ, Saigo H, Baldi P. Graph kernels for chemical informatics. Neural networks. 2005;18(8):1093-110.
48. Das B, Baidya AT, Chakrabarti S, Chouhan D, Thakur B, Darreh-Shori T, et al. Synthesis and biological evaluation of Halogen-Substituted novel α-Ketoamides as potential protein aggregation modulators in Alzheimer's disease. Bioorganic Chemistry. 2024;147:107373.